Comput Mech (2016) 57:37–53
DOI 10.1007/s00466-015-1220-8

ORIGINAL PAPER

Geometric non-linear hexahedral elements with rotational DOFs

Kamel Meftah[1] · **Wajdi Zouari**[2] · **Lakhdar Sedira**[3] · **Rezak Ayad**[4]

Received: 31 March 2015 / Accepted: 12 November 2015 / Published online: 25 November 2015

Abstract This paper presents an extension of two recently published conforming and non conforming eight-node hexahedral finite elements, presenting rotational degrees of freedom in addition to the classical displacement ones, to analyze geometric nonlinear problems. Their formulations are based on the so-called space fiber rotation concept that considers virtual rotations of a nodal fiber within the element which enhances the displacement vector approximation. To demonstrate the efficiency and accuracy of the proposed finite elements, several beam and shell nonlinear assessment tests are presented and the obtained results are principally compared with the classical first-order and second-order hexahedral elements responses as well as other advanced elements from the literature. In particular, it is shown that the proposed elements allow a correct prediction of the studied structures nonlinear behaviors including snap-through and snap-back instabilities and the accuracy of the non conforming element is close to the classical 20-node hexahedral element.

Keywords 3D hexahedral element · Rotational degrees of freedom · Geometric nonlinearity

1 Introduction

Nonlinear geometric analysis of structures represents one of the important items in their safe design as it allows, for example, predicting some serious problems like buckling instability. In fact, several lightweight structures like those used in aerospace applications can undergo large displacements even if the elastic limit of their constitutive materials are not reached [1]. In this case, the behavior of these structures is highly (geometrically) nonlinear and numerical approximation methods should be used for their study and optimization. Within this context, the finite element method has been widely considered to solve nonlinear geometric problems and several nonlinear elements have been developed throughout the past 30 years. These elements can be mainly classified into three categories: shell, solid-shell and three-dimensional (3D) solid finite elements.

Several three-node and four-node enhanced shell finite elements have been extended to describe large displacements and large rotations of shell structures (see [2–8] for four-node elements and [9–12] for three-node shell elements, among others). As displacement-based formulations suffer from many numerical pathologies like the so-called transverse shear locking, several nonlinear shell elements have been based on mixed variational formulations that result in some well known approaches like the so-called assumed natural strain (ANS) approach [2] or the enhanced assumed natural strain (EANS) method [13]. Besides, different strain measures have been used in nonlinear shell elements such as Green–Lagrange strains adopted in [3,14] or Biot strains considered in [4,5]. Despite these valuable contributions which are principally based on simplified assumptions across the thickness, modeling geometric nonlinear problems with shell finite elements could be insufficient in some cases especially when information across

---

✉ Wajdi Zouari
wajdi.zouari@univ-reims.fr

[1] Laboratoire de Génie Energétique et Matériaux, LGEM, University of Biskra, BP 145 RP, 07000 Biskra, Algeria

[2] University of Reims Champagne-Ardenne, LISM EA 4695, IUT de Troyes, 9 rue de Québec, 10026 Troyes, France

[3] Laboratoire de Génie Mécanique, LGM, University of Biskra, BP 145 RP, 07000 Biskra, Algeria

[4] University of Reims Champagne-Ardenne, LISM EA 4695, ESI Reims, Esplanade Roland Garros, 51100 Reims, France

the thickness direction is needed as in sheet metal forming simulations.

During the last 20 years, a consequent research effort has been devoted to develop the so-called solid-shell finite elements to model linear and especially nonlinear behaviors of thin to moderately thick structures (see [15–22] to cite only a few). These continuum-based elements offer many advantages with respect to shell elements such as the use of kinematics much easier than those of complex shell-type ones, the use of complete 3D constitutive laws, the direct determination of thickness variations as well as the simple connection with 3D solid elements since displacements are their only DOFs [20]. For instance, in the work of Abed-Meraim and Combescure [20], the under-integrated solid-shell element SHB8PS formulation was revised to eliminate some remaining membrane and shear locking problems. This element was used to analyze in particular some geometric nonlinear popular benchmarks and the obtained results were found to agree well with reference solutions.

3D enhanced solid elements have been also developed to analyze geometric nonlinear problems [1,6,23,24]. In the work of Ooi et al. [1], an extension of the unsymmetric 20-node hexahedral element US-HEXA20, based on the Petrov-Galerkin formulation, was proposed to account for geometrically nonlinear problems. Two different sets of shape functions, namely isoparametric and metric shape functions, were considered and the Total Lagrangian approach was adopted. To overcome numerical difficulties of the classical first-order hexahedral element, Klinkel and Wagner [23] developed a first-order 3D brick element based on the enhanced assumed strain method and 30 incompatible modes were considered to enhance the strain tensor. In addition to that, improvements of the classical low-order hexahedral element were reported by Reese in [25] for 3D finite elasto-plasticity (the under-integrated element Q1SPe was presented) and by Wang and Wagoner in [26] to analyze sheet metal forming problems (the eight-node hexahedral element WW3D was developed).

In this paper, we present an extension of two recently published 3D solid elements [27], named SFR8 and SFR8I, to account for geometrically nonlinear problems. Their formulations are based on the so-called space fiber rotation (SFR) concept firstly introduced by Ayad in [28]. This concept considers 3D rotations of a virtual fiber within the finite element that enhances the displacement vector approximation and subsequently the strain tensor expression. Consequently, the SFR concept introduces rotational DOFs in addition to the classical displacement ones. In Ayad et al. [27], the SFR concept was adopted to formulate the eight-node hexahedral elements SFR8 and SFR8I and linear benchmarks were considered to assess their responses. SFR8I is a nonconforming element because three incompatible modes are introduced in the element natural space to avoid the Poisson thickness locking encountered in bending-dominated situations. In particular, the SFR8 and especially SFR8I responses were shown to be much more accurate than the classical first-order hexahedral element and close to the quadratic 20-node hexahedral element with a quasi-insensitivity to high mesh distortions. Moreover, Meftah et al. [29] developed a six-node wedge element named SFR6 and based on the SFR concept for linear problems. In the same way as the SFR hexahedral elements, the SFR6 results were found to agree very well with reference solutions and its accuracy outweighs that of the first-order wedge element.

The present paper is structured as follows. In Sect. 2, the variational formulation of the nonlinear geometric problem based on the Total Lagrangian approach is recalled. Section 3 is devoted to the SFR concept finite element approximation by extending the formulations of the hexahedral elements SFR8 and SFR8I to geometric nonlinear problems as well as their implementation in the commercial code ABAQUS. Finally, and before the concluding remarks, the performance of the proposed nonlinear hexahedral elements is investigated by studying several beam and shell structures in Sect. 4.

2 Total Lagrangian formulation

Consider a 3D deformable body undergoing large displacements. The Total Lagrangian approach is adopted to describe its motion and the initial undeformed configuration C_0 is fixed as the reference configuration (Fig. 1). Suppose that the total load subjected to this body is applied in several increments so that the body occupies intermediate configurations before converging to the final one. Consequently, the equilibrium of this body must be solved for each loading increment. Consider for this the loading interval $[t_n, t_{n+1}]$ and denote with the indexes n and $n+1$ all quantities at t_n and t_{n+1}, respectively. We assume that the body is in equilibrium at $t = t_n$ and hence the configuration C_n is known. An increment of the external load results in an increment of the displacement vector between the configurations C_n and C_{n+1}. We denote by $C_{n+1}^{(k)}$ the last known configuration between C_n and C_{n+1} that does not verify the body equilibrium. A correction of the displacement vector $\triangle \underline{u}^{(k)}$ should be determined to reach the next configuration $C_{n+1}^{(k+1)}$. For this last configuration, the weak form of the equilibrium reads [30]:

$$\begin{aligned}\delta\pi =& \int_{{}^0V} {}^{n+1}_{\;\;\,0}S_{ij}^{(k+1)}\, \delta\big({}^{n+1}_{\;\;\,0}E_{ij}^{(k+1)}\big)\, d\,{}^0V \\ &- \underbrace{\Big[\int_{{}^0S} {}^{n+1}_{\;\;\,0}T_i\, \delta u_i\, d\,{}^0S + \int_{{}^0V} {}^{n+1}_{\;\;\,0}f_i^v\, \delta u_i\, d\,{}^0V\Big]}_{\delta({}^{n+1}_{\;\;\,0}W_{ext})} = 0\end{aligned} \tag{1}$$

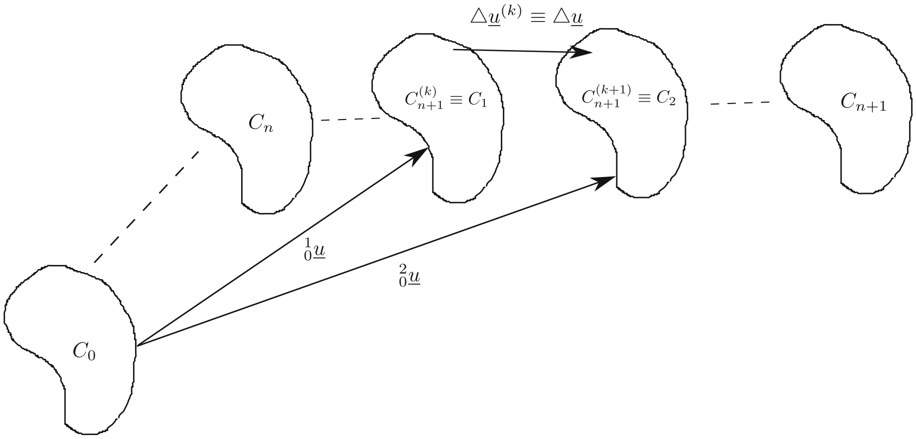

Fig. 1 Reference and deformed configurations of the elastic body

where ${}^{n+1}_{0}\underline{T}$ and ${}^{n+1}_{0}\underline{f}^{v}$ are, respectively, the boundary traction forces and the body forces applied to C_{n+1} and referred to the reference configuration C_0, $\underline{\underline{S}}$ and $\underline{\underline{E}}$ are, respectively, the second Piola–Kirchoff stress tensor and the Green–Lagrange strain tensor, and $\delta({}^{n+1}_{0}W_{ext})$ denotes the virtual work done by the external loads.

To simplify, we adopt the following notation:

$$\begin{array}{lll}
{}^{n+1}_{0}S^{(k)}_{ij} = {}^{1}_{0}S_{ij} & ; & {}^{n+1}_{0}E^{(k)}_{ij} = {}^{1}_{0}E_{ij} \\
{}^{n+1}_{0}S^{(k+1)}_{ij} = {}^{2}_{0}S_{ij} & ; & {}^{n+1}_{0}E^{(k+1)}_{ij} = {}^{2}_{0}E_{ij} \\
{}^{n+1}_{0}u^{(k)}_{i} = {}^{1}_{0}u_{i} & ; & {}^{n+1}_{0}u^{(k+1)}_{i} = {}^{2}_{0}u_{i} \\
\triangle\underline{u}^{(k)} = \triangle\underline{u} & &
\end{array} \tag{2}$$

Equation (1) can thus be rewritten as:

$$\delta\pi = \int_{{}^0V} {}^{2}_{0}S_{ij}\,\delta\big({}^{2}_{0}E_{ij}\big)\,d\,{}^0V - \delta\big({}^{n+1}_{0}W_{ext}\big) = 0 \tag{3}$$

By remarking that

$$\begin{aligned}
&{}^{2}_{0}u_{i} = {}^{1}_{0}u_{i} + \triangle u_i; \quad {}^{2}_{0}E_{ij} = {}^{1}_{0}E_{ij} + \triangle E_{ij}; \\
&{}^{2}_{0}S_{ij} = {}^{1}_{0}S_{ij} + \triangle S_{ij}
\end{aligned} \tag{4}$$

where $\triangle E_{ij}$ and $\triangle S_{ij}$ are, respectively, the Green–Lagrange strain and Kirchoff stress increments between $C^{(k)}_{n+1}$ and $C^{(k+1)}_{n+1}$, we arrive at the following expression:

$$\begin{aligned}
&\int_{{}^0V} {}^{1}_{0}S_{ij}\,\delta(\triangle E_{ij})\,d\,{}^0V + \int_{{}^0V} \triangle S_{ij}\,\delta(\triangle\, E_{ij})\,d\,{}^0V \\
&\quad - \delta\big({}^{n+1}_{0}W_{ext}\big) = 0
\end{aligned} \tag{5}$$

${}^{1}_{0}\underline{\underline{S}}$ and ${}^{1}_{0}\underline{\underline{E}}$ are given by (the Einstein summation technique is used):

$$\begin{aligned}
{}^{1}_{0}S_{ij} &= C_{ijkl}\,{}^{1}_{0}E_{kl}; \\
{}^{1}_{0}E_{ij} &= \frac{1}{2}\left(\frac{\partial\,{}^{1}_{0}u_i}{\partial x_j} + \frac{\partial\,{}^{1}_{0}u_j}{\partial x_i} + \frac{\partial\,{}^{1}_{0}u_k}{\partial x_i}\cdot\frac{\partial\,{}^{1}_{0}u_k}{\partial x_j}\right)
\end{aligned} \tag{6}$$

where C_{ijkl} are the components of the elasticity tensor and x_i $(i = 1, 2, 3)$ are the cartesian coordinates of the reference configuration C_0.

The increment of the Green–Lagrange strain tensor $\triangle\underline{\underline{E}}$ can be decomposed into linear $\triangle\underline{\underline{e}}$ and nonlinear $\triangle\underline{\underline{\eta}}$ strain tensors in term of the unknown displacement vector $\triangle\underline{u}$ [30]:

$$\begin{aligned}
\triangle e_{ij} &= \frac{1}{2}\left(\frac{\partial\triangle u_i}{\partial x_j} + \frac{\partial\triangle u_j}{\partial x_i} + \frac{\partial\,{}^{1}_{0}u_k}{\partial x_i}\cdot\frac{\partial\triangle u_k}{\partial x_j} + \frac{\partial\,{}^{1}_{0}u_k}{\partial x_j}\cdot\frac{\partial\triangle u_k}{\partial x_i}\right) \\
\triangle\eta_{ij} &= \frac{1}{2}\,\frac{\partial\triangle u_k}{\partial x_i}\cdot\frac{\partial\triangle u_k}{\partial x_j}
\end{aligned} \tag{7}$$

The variations of $\triangle\underline{\underline{e}}$ and $\triangle\underline{\underline{\eta}}$ are given by:

$$\begin{aligned}
\delta(\triangle e_{ij}) &= \frac{1}{2}\left(\frac{\partial\delta u_i}{\partial x_j} + \frac{\partial\delta u_j}{\partial x_i} + \frac{\partial\,{}^{1}_{0}u_k}{\partial x_i}\cdot\frac{\partial\delta u_k}{\partial x_j} + \frac{\partial\,{}^{1}_{0}u_k}{\partial x_j}\cdot\frac{\partial\delta u_k}{\partial x_i}\right) \\
\delta(\triangle\eta_{ij}) &= \frac{1}{2}\left(\frac{\partial\triangle u_k}{\partial x_i}\cdot\frac{\partial\delta u_k}{\partial x_j} + \frac{\partial\delta u_k}{\partial x_i}\cdot\frac{\partial\triangle u_k}{\partial x_j}\right)
\end{aligned} \tag{8}$$

After conserving all terms related to the unknown displacement vector $\triangle\underline{u}$ on the left hand side of the weak form (5), this last expression becomes:

$$\begin{aligned}
&\int_{{}^0V} \triangle S_{ij}\,\delta(\triangle E_{ij})\,d\,{}^0V + \int_{{}^0V} {}^{1}_{0}S_{ij}\,\delta(\triangle\eta_{ij})\,d\,{}^0V \\
&\quad = \; -\int_{{}^0V} {}^{1}_{0}S_{ij}\,\delta(\triangle e_{ij})\,d\,{}^0V + \delta({}^{n+1}_{0}W_{ext})
\end{aligned} \tag{9}$$

After that, it is supposed that the displacement vector $\triangle\underline{u}$ is small enough so that the following approximation can hold as explained in [30]:

$$\triangle S_{ij}\,\delta(\triangle E_{ij}) \approx C_{ijkl}\triangle e_{kl}\,\delta(\triangle e_{ij}) \tag{10}$$

We obtain hence the final weak form to develop the finite element approximation based on the Total Lagrangian formulation:

$$\int_{{}^0V} C_{ijkl}\triangle e_{kl}\,\delta(\triangle e_{ij})\,d\,{}^0V + \int_{{}^0V} {}^1_0S_{ij}\,\delta(\triangle\eta_{ij})\,d\,{}^0V$$
$$= -\int_{{}^0V} {}^1_0S_{ij}\,\delta(\triangle e_{ij})\,d\,{}^0V + \delta({}^{n+1}_{0}W_{ext}) \qquad (11)$$

This will be developed in the next section by presenting the formulations of two conforming and non conforming eight-node hexahedral elements with rotational DOFs.

3 The SFR concept finite element approximation

3.1 Formulation of the conforming element SFR8

The finite element approximation of Eq. (11) is constructed by dividing the 3D deformable body into elementary domains or finite elements. In order to analyze geometric nonlinear problems, the formulations of two recently published hexahedral elements, named respectively SFR8 and SFR8I [27], are extended in this paper within the Total Lagrangian framewok. They are based on the so-called SFR concept initially proposed by Ayad in [28]. As shown in Fig. 2, this concept considers 3D rotations of a virtual nodal fiber within the element (fiber $\underline{iq}$ in Fig. 2a) that enhances the classical approximation of the displacement vector. As proposed in [27,28], the SFR approximation of the displacement vector of one point q of the element is given by:

$$\underline{u}(\xi,\eta,\zeta)=\sum_{i=1}^{8} N_i(\xi,\eta,\zeta)\left(\underline{u}_i + \underline{\theta}_i \wedge \underline{iq}\right); \quad \underline{u}_q \equiv \underline{u} \qquad (12)$$

where N_i are the classical trilinear Lagrange interpolation functions associated with the eight-node hexahedral element, $\{u_i\} = \{u_i\ v_i\ w_i\}^T$ is the vector of nodal displacements and $\{\theta_i\} = \{\theta_{xi}\ \theta_{yi}\ \theta_{zi}\}^T$ is the vector of nodal virtual rotations.

Equation (12) can be rewritten in the following matrix form:

$$\{u\} = [N]\,\{u_n^e\} \quad ; \quad [N] = \begin{bmatrix} & \{N_{ui}\}^T & \\ \cdots & \{N_{vi}\}^T & \cdots i=1,8 \\ & \{N_{wi}\}^T & \end{bmatrix}$$
$$= \begin{bmatrix} \{N_u\}^T \\ \{N_v\}^T \\ \{N_w\}^T \end{bmatrix} \qquad (13)$$

where

$$\begin{aligned} \{N_{ui}\} &= \{\ N_i\ \ 0\ \ 0 \vdots\ \ 0\ \ \vdots\ N_i(z-z_i)\ \vdots -N_i(y-y_i)\ \}^T \\ \{N_{vi}\} &= \{\ 0\ \ N_i\ \ 0 \vdots -N_i(z-z_i) \vdots\ \ 0\ \ \vdots\ N_i(x-x_i)\ \}^T \\ \{N_{wi}\} &= \{\ 0\ \ 0\ \ N_i \vdots\ N_i(y-y_i) \vdots -N_i(x-x_i) \vdots\ \ 0\ \ \}^T \end{aligned} \qquad (14)$$

and

$$\{u_n^e\} = \{\cdots \mid u_i\ v_i\ w_i \vdots \theta_{xi}\ \theta_{yi}\ \theta_{zi} \mid \cdots i=1,8\}^T \qquad (15)$$

is the elementary nodal DOFs vector containing the nodal displacements and fictive rotations.

We introduce at this stage the notation

$${}^1_0u_1 = u, \quad {}^1_0u_2 = v, \quad {}^1_0u_3 = w, \quad \triangle u_1 = \triangle u,$$
$$\triangle u_2 = \triangle v, \quad \triangle u_3 = \triangle w \qquad (16)$$

At the element level, the first term of Eq. (11) is written in the alternate form

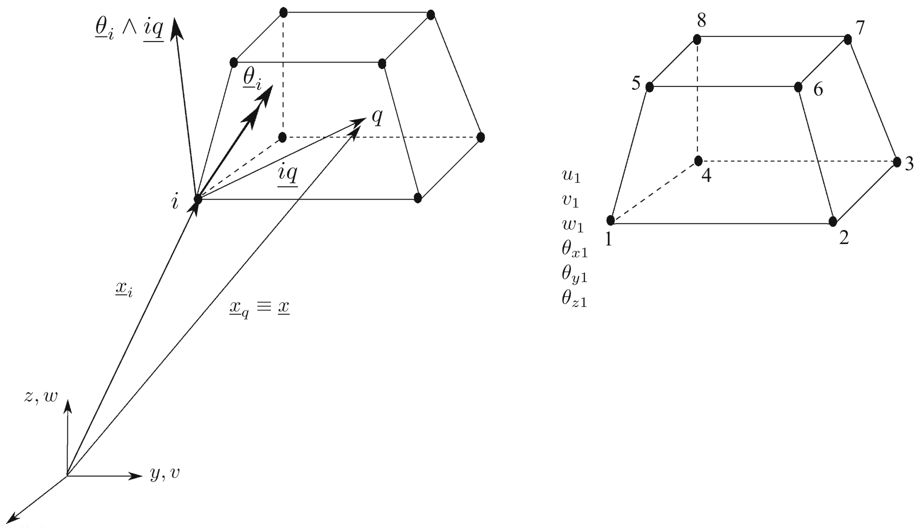

(a) (b)

Fig. 2 The SFR concept. **a** 3D rotation $\underline{\theta}_i$ of the virtual nodal fiber $\underline{iq}$ inducing an additional displacement $\underline{\theta}_i \wedge \underline{iq}$. **b** The hexahedral element SFR8 and its nodal degrees of freedom

$$\int_{{}^0V} C_{ijkl}\triangle e_{kl}\,\delta(\triangle e_{ij})\,d\,{}^0V = \int_{{}^0V}\{\delta\triangle e\}^T[C]\{\triangle e\}\,d\,{}^0V \tag{17}$$

where $[C]$ is the elasticity matrix and $\{\triangle e\} = \{\triangle e_{xx}\ \triangle e_{yy}\ \triangle e_{zz}\ 2\triangle e_{xy}\ 2\triangle e_{xz}\ 2\triangle e_{yz}\}^T$.

Using Eq. (7), $\{\triangle e\}$ can be shown to be related to $\{\triangle u_n^e\}$ by a (6×48)-sized matrix $[B_L]$ as:

$$\{\triangle e\} = [B_L]\{\triangle u_n^e\},\quad [B_L] = [B_{L0}] + [B_{L1}] \tag{18}$$

where

$$[B_{L0}] = [D_0].[N]\ \ ;\ \ [D_0] = \begin{bmatrix} \frac{\partial}{\partial x} & 0 & 0 \\ 0 & \frac{\partial}{\partial y} & 0 \\ 0 & 0 & \frac{\partial}{\partial z} \\ \frac{\partial}{\partial y} & \frac{\partial}{\partial x} & 0 \\ \frac{\partial}{\partial z} & 0 & \frac{\partial}{\partial x} \\ 0 & \frac{\partial}{\partial z} & \frac{\partial}{\partial y} \end{bmatrix} \tag{19}$$

and

$$[B_{L1}] = [D_1].[N]\ \ ;$$

$$[D_1] = \begin{bmatrix} \frac{\partial u}{\partial x}\cdot\frac{\partial}{\partial x} & \frac{\partial v}{\partial x}\cdot\frac{\partial}{\partial x} & \frac{\partial w}{\partial x}\cdot\frac{\partial}{\partial x} \\ \frac{\partial u}{\partial y}\cdot\frac{\partial}{\partial y} & \frac{\partial v}{\partial y}\cdot\frac{\partial}{\partial y} & \frac{\partial w}{\partial y}\cdot\frac{\partial}{\partial y} \\ \frac{\partial u}{\partial z}\cdot\frac{\partial}{\partial z} & \frac{\partial v}{\partial z}\cdot\frac{\partial}{\partial z} & \frac{\partial w}{\partial z}\cdot\frac{\partial}{\partial z} \\ \frac{\partial u}{\partial x}\cdot\frac{\partial}{\partial y}+\frac{\partial u}{\partial y}\cdot\frac{\partial}{\partial x} & \frac{\partial v}{\partial x}\cdot\frac{\partial}{\partial y}+\frac{\partial v}{\partial y}\cdot\frac{\partial}{\partial x} & \frac{\partial w}{\partial x}\cdot\frac{\partial}{\partial y}+\frac{\partial w}{\partial y}\cdot\frac{\partial}{\partial x} \\ \frac{\partial u}{\partial x}\cdot\frac{\partial}{\partial z}+\frac{\partial u}{\partial z}\cdot\frac{\partial}{\partial x} & \frac{\partial v}{\partial x}\cdot\frac{\partial}{\partial z}+\frac{\partial v}{\partial z}\cdot\frac{\partial}{\partial x} & \frac{\partial w}{\partial x}\cdot\frac{\partial}{\partial z}+\frac{\partial w}{\partial z}\cdot\frac{\partial}{\partial x} \\ \frac{\partial u}{\partial y}\cdot\frac{\partial}{\partial z}+\frac{\partial u}{\partial z}\cdot\frac{\partial}{\partial y} & \frac{\partial v}{\partial y}\cdot\frac{\partial}{\partial z}+\frac{\partial v}{\partial z}\cdot\frac{\partial}{\partial y} & \frac{\partial w}{\partial y}\cdot\frac{\partial}{\partial z}+\frac{\partial w}{\partial z}\cdot\frac{\partial}{\partial y} \end{bmatrix} \tag{20}$$

More details about $[B_{L0}]$ and $[B_{L1}]$ components are found in Appendix.

Using relation (18), the first term of the weak form (11) is then given by:

$$\int_{{}^0V} C_{ijkl}\triangle e_{kl}\,\delta(\triangle e_{ij})\,d\,{}^0V = \{\delta\triangle u_n^e\}^T \underbrace{\int_{{}^0V}[B_L]^T[C][B_L]\,d\,{}^0V}_{[K_L^e]}\{\triangle u_n^e\} \tag{21}$$

where $[K_L^e]$ is the elementary linear stiffness matrix of SFR8.

At the element level, the second term of Eq. (11) can be rewritten as [30]:

$$\begin{aligned}\int_{{}^0V} {}^1_0S_{ij}\,\delta(\triangle\eta_{ij})\,d\,{}^0V &= \int_{{}^0V}\{\delta\triangle\eta\}^T\{{}^1_0S\}\,d\,{}^0V \\ &= \int_{{}^0V}\begin{Bmatrix}\delta\triangle u\\ \delta\triangle v\\ \delta\triangle w\end{Bmatrix}^T [D_{NL}]^T[{}^1_0S][D_{NL}]\begin{Bmatrix}\triangle u\\ \triangle v\\ \triangle w\end{Bmatrix} d\,{}^0V\end{aligned} \tag{22}$$

where $\{\triangle\eta\} = \{\triangle\eta_{xx}\ \triangle\eta_{yy}\ \triangle\eta_{zz}\ 2\triangle\eta_{xy}\ 2\triangle\eta_{xz}\ 2\triangle\eta_{yz}\}^T$,

$$[D_{NL}]^T = \begin{bmatrix} \frac{\partial}{\partial x} & \frac{\partial}{\partial y} & \frac{\partial}{\partial z} & 0 & 0 & 0 & 0 & 0 & 0 \\ 0 & 0 & 0 & \frac{\partial}{\partial x} & \frac{\partial}{\partial y} & \frac{\partial}{\partial z} & 0 & 0 & 0 \\ 0 & 0 & 0 & 0 & 0 & 0 & \frac{\partial}{\partial x} & \frac{\partial}{\partial y} & \frac{\partial}{\partial z} \end{bmatrix} \tag{23}$$

and

$$[{}^1_0S] = \begin{bmatrix} {}^1_0S_{xx} & {}^1_0S_{xy} & {}^1_0S_{xz} & 0 & 0 & 0 & 0 & 0 & 0 \\ {}^1_0S_{xy} & {}^1_0S_{yy} & {}^1_0S_{yz} & 0 & 0 & 0 & 0 & 0 & 0 \\ {}^1_0S_{xz} & {}^1_0S_{yz} & {}^1_0S_{zz} & 0 & 0 & 0 & 0 & 0 & 0 \\ 0 & 0 & 0 & {}^1_0S_{xx} & {}^1_0S_{xy} & {}^1_0S_{xz} & 0 & 0 & 0 \\ 0 & 0 & 0 & {}^1_0S_{xy} & {}^1_0S_{yy} & {}^1_0S_{yz} & 0 & 0 & 0 \\ 0 & 0 & 0 & {}^1_0S_{xz} & {}^1_0S_{yz} & {}^1_0S_{zz} & 0 & 0 & 0 \\ 0 & 0 & 0 & 0 & 0 & 0 & {}^1_0S_{xx} & {}^1_0S_{xy} & {}^1_0S_{xz} \\ 0 & 0 & 0 & 0 & 0 & 0 & {}^1_0S_{xy} & {}^1_0S_{yy} & {}^1_0S_{yz} \\ 0 & 0 & 0 & 0 & 0 & 0 & {}^1_0S_{xz} & {}^1_0S_{yz} & {}^1_0S_{zz} \end{bmatrix} \tag{24}$$

Using the approximation matrix $[N]$ and the transformation (22), the second term of the weak form (11) becomes:

$$\int_{{}^0V} {}^1_0S_{ij}\,\delta(\triangle\eta_{ij})d\,{}^0V = \{\delta\triangle u_n^e\}^T\underbrace{\int_{{}^0V}[B_{NL}]^T[{}^1_0S][B_{NL}]\,d\,{}^0V}_{[K_{NL}^e]}\{\triangle u_n^e\} \tag{25}$$

where $[B_{NL}] = [D_{NL}][N]$ and $[K_{NL}^e]$ is the elementary nonlinear stiffness matrix of SFR8. More details about $[B_{NL}]$ components are found in Appendix.

Using Eq. (18), the third term of the weak form (11) is rewritten in a matrix form as:

$$\int_{{}^0V} {}^1_0S_{ij}\,\delta(\triangle e_{ij})\,d\,{}^0V = \{\delta\triangle u_n^e\}^T\int_{{}^0V}[B_L]^T\{{}^1_0S\}\,d\,{}^0V \tag{26}$$

where $\{{}^1_0S\} = \{{}^1_0S_{xx}\ {}^1_0S_{yy}\ {}^1_0S_{zz}\ {}^1_0S_{xy}\ {}^1_0S_{xz}\ {}^1_0S_{yz}\}^T$.

At the element level, the substitution of Eqs. (21), (25) and (26) into Eq. (11) yields the finite element model to determine the correction $\{\triangle u_n^e\}$:

$$\Big(\underbrace{[K_L^e]+[K_{NL}^e]}_{[K_T^e]}\Big)\{\triangle u_n^e\} = \underbrace{-\int_{^0V}[B_L]^T\{{}^1_0S\}\,d\,{}^0V+\{{}^{n+1}_{0}F^e_{ext}\}}_{\{R^e\}} \tag{27}$$

where $\{{}^{n+1}_{0}F^e_{ext}\} = \int_{^0V}[N]^T\{{}^{n+1}_{0}f^v\}\,d\,{}^0V + \int_{^0S}[N]^T\{{}^{n+1}_{0}T\}\,d\,{}^0S$ is the vector of external loads, $[K_T^e]$ is the elementary tangent stiffness matrix and $\{R^e\}$ is the elementary residual vector.

3.2 Formulation of the non conforming element SFR8I

In this section, we present the nonlinear formulation of the non conforming element SFR8I based on the Total Lagrangian approach. As explained in [27], three incompatible displacement modes a_u, a_v and a_w are introduced in the natural space of the element to prevent the Poisson's ratio locking. The natural space extra modes are given as [27]:

$$\begin{cases} u^a = (1-\xi^2)\,a_u \\ v^a = (1-\eta^2)\,a_v \\ w^a = (1-\zeta^2)\,a_w \end{cases} \tag{28}$$

In this case, we obtain an enhanced Green–Lagrange strain vector:

$$\{E\} = \{E^u\}+\{E^a\}, \quad \{E^a\} = [M^a]\{a\} \tag{29}$$

where $\{E^u\}$ and $\{E^a\}$ are, respectively, the conforming and non conforming strain vectors, $\{a\}$ is the vector of incompatible modes and $[M^a]$ the matrix relating $\{E^a\}$ to $\{a\}$ (see [27] for more details about $[M^a]$).

After introducing the enhanced strain vector in the equilibrium weak form (5) at the element level instead of the compatible strain vector, we obtain the following system of equations [16,17,23,31]:

$$\begin{bmatrix} [K_L^e]+[K_{NL}^e] & [K_{ua}^e] \\ [K_{au}^e] & [K_{aa}^e] \end{bmatrix} \begin{Bmatrix} \{\triangle u_n^e\} \\ \{\triangle a\} \end{Bmatrix} = \begin{Bmatrix} \{{}^{n+1}_{0}F^e_{ext}\} - \int_{^0V}[B_L]^T\{{}^1_0S\}\,d\,{}^0V \\ -\int_{^0V}[M^a]^T\{{}^1_0S\}\,d\,{}^0V \end{Bmatrix} \tag{30}$$

where

$$[K_{ua}^e] = \int_{^0V}[B_L]^T[C][M^a]\,d\,{}^0V, \qquad [K_{au}^e] = [K_{ua}^e]^T,$$
$$[K_{aa}^e] = \int_{^0V}[M^a]^T[C][M^a]\,d\,{}^0V \tag{31}$$

The vector of internal variables $\{\triangle a\}$ can be eliminated at the element level by using a static condensation. We obtain

$$\{\triangle a\} = -[K_{aa}^e]^{-1}\Big([K_{au}^e]\{\triangle u_n^e\} + \int_{^0V}[M^a]^T\{{}^1_0S\}\,d\,{}^0V\Big) \tag{32}$$

Finally, the following system of equations should be solved to determine the correction $\{\triangle u_n^e\}$ for SFR8I:

$$[K_T^e]\{\triangle u_n^e\} = \{R^e\} \tag{33}$$

with

$$[K_T^e] = [K_L^e]+[K_{NL}^e]-[K_{ua}^e][K_{aa}^e]^{-1}[K_{au}^e] \tag{34}$$

$$\{R^e\} = \{{}^{n+1}_{0}F^e_{ext}\} - \int_{^0V}[B_L]^T\{{}^1_0S\}\,d\,{}^0V + [K_{ua}^e][K_{aa}^e]^{-1}\int_{^0V}[M^a]^T\{{}^1_0S\}\,d\,{}^0V \tag{35}$$

3.3 Implementation in ABAQUS

The SFR concept-based finite elements SFR8 and SFR8I were implemented in the commercial code ABAQUS via the user element subroutine (UEL) [32]. We depict in Fig. 3 the general resolution scheme of the geometric nonlinear problem in ABAQUS via UEL for the conforming element SFR8. At the element level, we should

1. First, construct the elementary stiffness matrix $[K_T^e]$ that will be stored in the predefined matrix AMATRX of ABAQUS;
2. and second, compute the elementary residual vector $\{R^e\}$ which will be stored in the predefined right hand side vector RHS.

4 Numerical validation

The performances of the proposed SFR concept hexahedral elements, for geometric nonlinear problems, are evaluated with several known beam and shell benchmarks. The obtained results of SFR8 and SFR8I are then compared with some advanced elements from the literature as well as the ABAQUS hexahedral elements C3D8 and C3D20 [32]:

- C3D8: the classical eight-node first-order hexahedral element with an exact numerical integration scheme;
- C3D20: the classical 20-node second-order hexahedral element with an exact numerical integration scheme.

It is worth noting that in ABAQUS Standard, C3D8 and C3D20 are formulated in the current configuration when

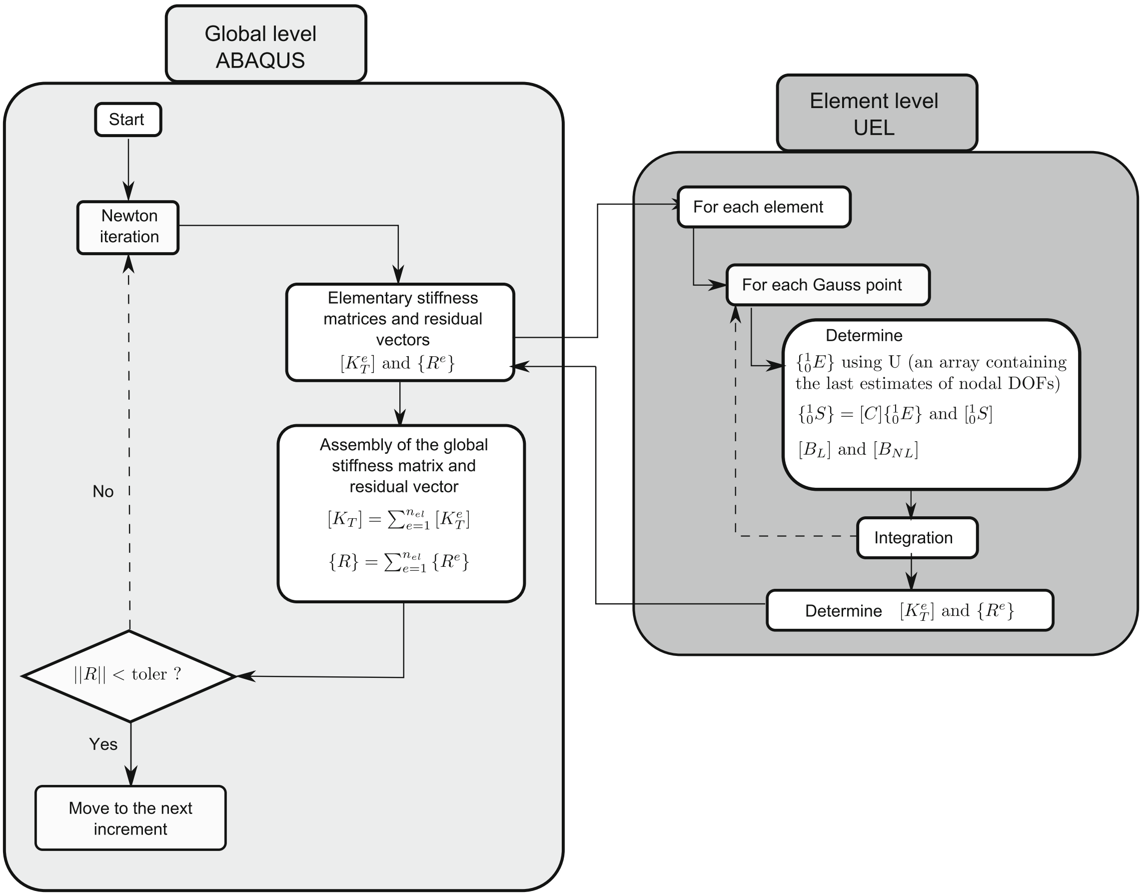

Fig. 3 Resolution of the geometric nonlinear problem in ABAQUS using the UEL subroutine

Fig. 4 A cantilever beam subjected to an end shear force modeled with the regular mesh $10 \times 1 \times 1$

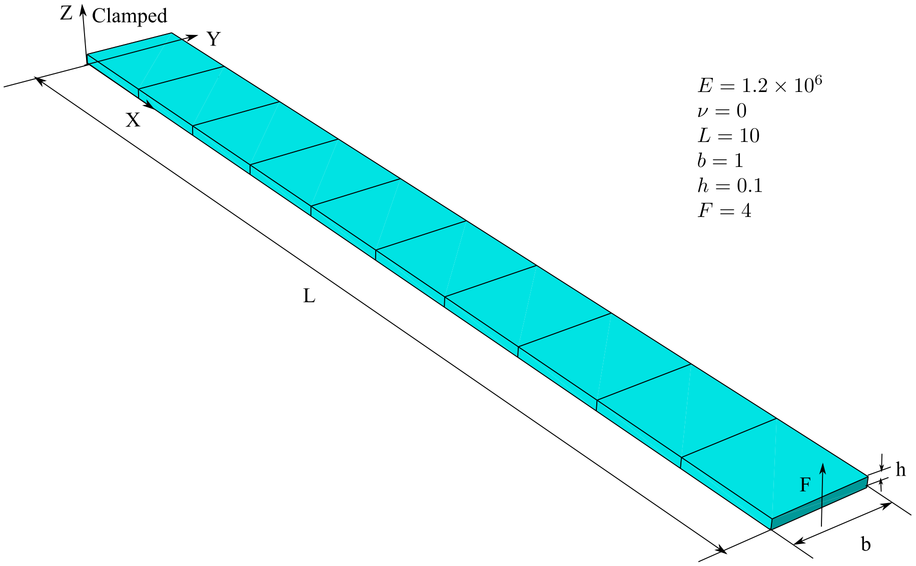

the NLGEOM option is specified in the input file [32]. The nonlinear solution procedure adopted to solve the following problems is the full Newton–Raphson method and the default automatic load incrementation scheme in ABAQUS is used. The maximum applied load is automatically subdivided into NINC load increments that are not necessarily uniform. On the other hand, and in order to show the impact of the load step size on the accuracy of SFR8 and SFR8I, schemes with uniform load increments are also used in examples 4.1 and 4.3. Therefore, the maximum load is divided into a number

Table 1 The cantilever rectangular beam

	C3D8	C3D20	SFR8	SFR8I
NINC	7	10	12	10
NITER	8	56	49	71

The numbers of increments NINC and iterations NITER required to reach the ultimate solution with the automatic load incrementation scheme

of equal increments $\text{NINC}^\star$ which is much more larger than the number of increments NINC required by the automatic incrementation scheme.

For the different boundary conditions considered in the next sub-sections, it is worthy to note that constraints on the rotational DOFs should be added to the classical displacement ones as explained in [27].

4.1 A cantilever beam subjected to transverse bending

A rectangular cantilever beam subjected to an out-of-plane shear force at its free end is studied in this example (Fig. 4). Reference solutions of the tip displacements along the X and Z directions are reported by Sze et al. [33] by considering two converged meshes (8×1 and 16×2) of the under-integrated first-order shell element of ABAQUS S4R. As shown in Fig. 4, this rectangular beam is modeled with the regular mesh $10 \times 1 \times 1$ and the automatic incrementation scheme is adopted. We summarize in Table 1 the total numbers of increments NINC and iterations NITER required to obtain the ultimate solution and depict in Fig. 5 the obtained results of SFR8 and SFR8I compared to C3D8 and C3D20. We show also in Fig. 6 the convergence of the normalized tip transverse displacement at maximum load ($F = 4$) with respect to the total number of variables in the model (DOFs plus internal variables) by considering the regular meshes $10 \times 1 \times 1$, $20 \times 2 \times 1$ and $40 \times 4 \times 1$. Furthermore, and in order to evaluate the impact of the load step size on the proposed SFR elements accuracy, we depict in Fig. 7 the load-displacement curves of SFR8 and SFR8I obtained by the automatic load incrementation scheme and a 40 equal load increments scheme ($\text{NINC}^\star = 40$).

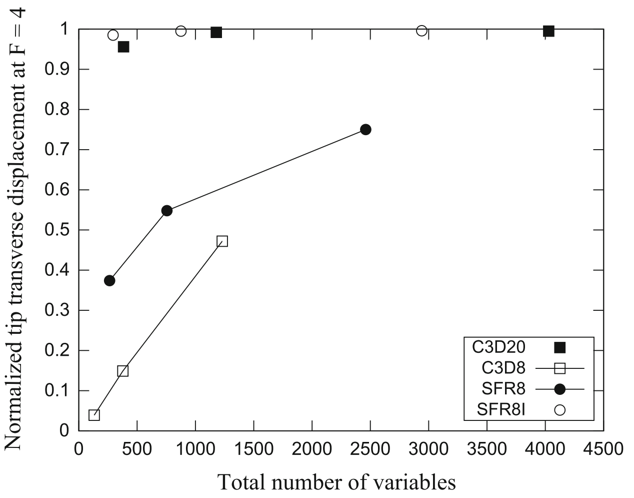

Fig. 6 The cantilever rectangular beam. Convergence of the normalized tip transverse displacement at $F = 4$ with respect to the total number of variables in the model ($w^{ref} = 6.698$ [33])

We remark that SFR8 clearly enhances the result of the first-order element C3D8 especially for the displacement along the Z direction but remains relatively far out the reference solution of Sze et al. [33] for the regular mesh $10 \times 1 \times 1$. The non conforming element SFR8I results agree very well

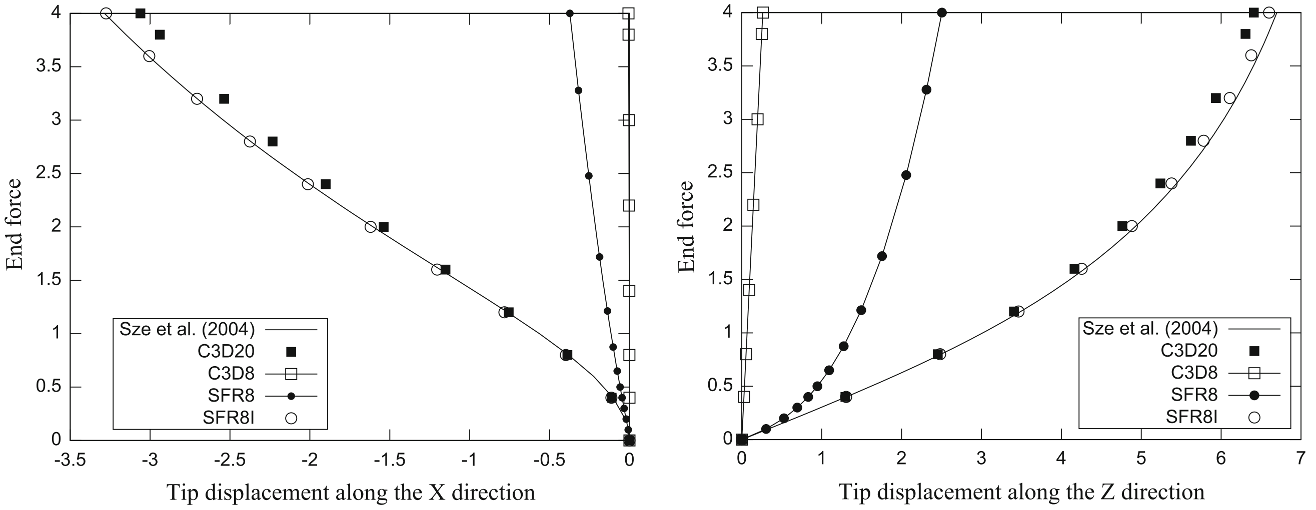

(a) **(b)**

Fig. 5 The cantilever rectangular beam. **a** Load versus displacement along the X direction curve and **b** Load versus displacement along the Z direction curve

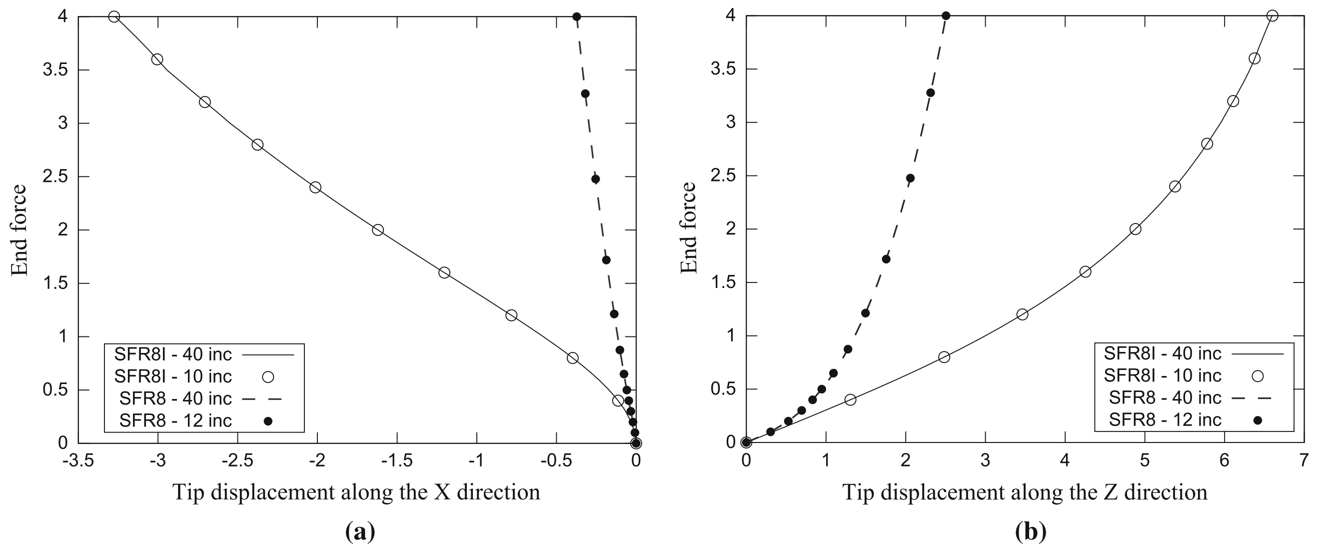

Fig. 7 The cantilever rectangular beam meshed with 10 × 1 × 1 elements. Impact of the load step size on the SFR8 and SFR8I results: **a** load versus displacement along the X direction curve and **b** load versus displacement along the Z direction curve

Fig. 8 A curved cantilever beam subjected to an end load modeled with the regular mesh 16 × 1 × 1

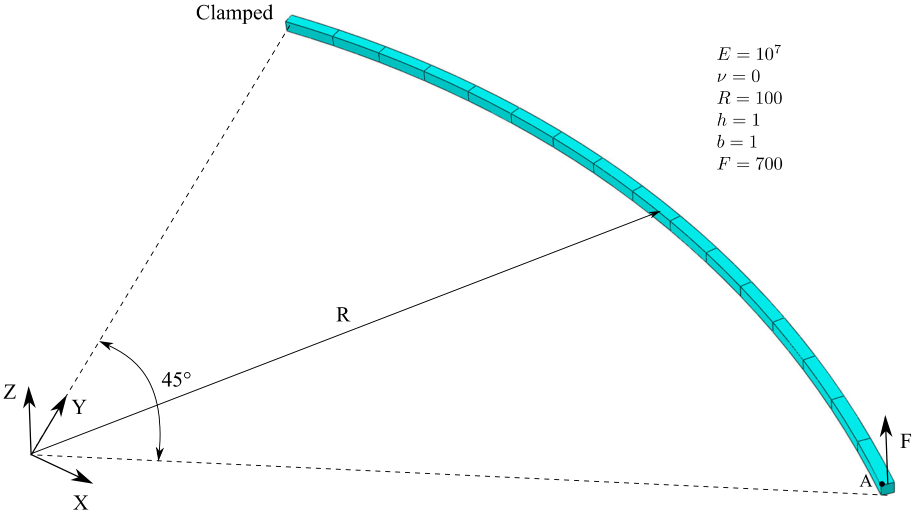

with the reference curves and are found to be more accurate than those of the quadratic element C3D20 (Fig. 5). From Fig. 7, we conclude that the SFR8 and SFR8I responses are practically not sensitive to the load step size as the same results are found with the automatic load incrementation scheme (limited number of increments) and the second 40 equal increments scheme.

4.2 Out-of-plane bending of a 45° circular cantilever beam

We consider in this example the 45° curved beam of Fig. 8 subjected to a concentrated end load. As considered in the works of Slavkovic et al. [6] and Klinkel and Wagner [23], this cantilever beam is modeled with the regular mesh 16×1×1. We show in Table 2 the total numbers of increments NINC and iterations NITER required to obtain the ultimate solution for C3D8, C3D20, SFR8 and SFR8I. The obtained load-tip displacements along X, Y and Z directions curves of SFR8 and SFR8I are compared to C3D8, C3D20 and the enhanced 3D hexahedral element Q1/E30 of Klinkel and Wagner [23] as shown in Fig. 9.

Table 2 The circular cantilever beam

	C3D8	C3D20	SFR8	SFR8I
NINC	7	13	9	10
NITER	25	61	50	62

The total numbers of increments NINC and iterations NITER required to reach the ultimate solution with the automatic load incrementation scheme

Once again, the results of SFR8I agree well with those of C3D20 and the enhanced solid element Q1/E30. The solution

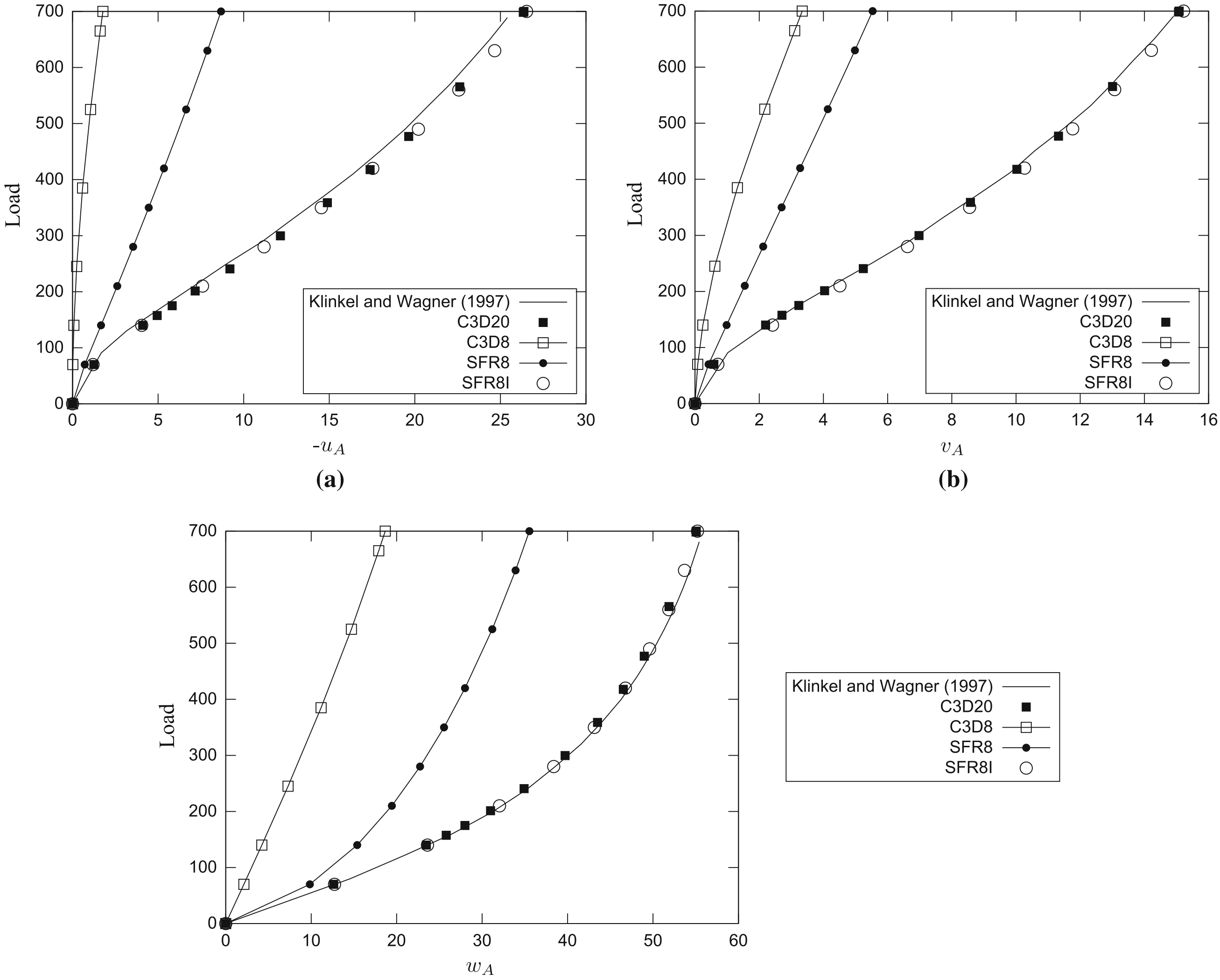

(a) (b) (c)

Fig. 9 Load-displacement curves of the circular cantilever beam

of SFR8 is more accurate than that of C3D8 but remains far out the other considered elements.

4.3 Pullout of an open-ended cylindrical shell

An open thin-walled cylinder of length $L = 10.35$ and radius $R = 4.953$ loaded by two opposite concentrated loads is studied in this example. This benchmark is considered in the literature as one of the most demanding tests for the geometrically nonlinear analysis of shells [1,33]. Thanks to the symmetry of the problem, only one-eighth of the cylinder is modeled with the regular mesh $8 \times 12 \times 1$ (Fig. 10) as considered in the works of Ooi et al. [1] and Sze et al. [34]. The loading applied to the cylinder shell is increased up to a maximum load $P = 18{,}000$. A reference solution of the vertical displacement at the point of load application (point A) is reported by Sze et al. in [33] by considering two converged meshes (16×24 and 24×36) of the shell element S4R. We list in Table 3 the total numbers of increments NINC and iterations NITER required to obtain the ultimate solution and depict in Fig. 11 the load-deflection curves of SFR8 and SFR8I along with those of C3D8, C3D20, the unsymmetric 20-node hexahedral element US-HEXA20 of Ooi et al. [1] and the eight-node hybrid-stress solid-shell element HS of Sze et al. [34]. We show also in Fig. 12 the convergence of the normalized displacement of point A at maximum load ($P = 18, 000$) with respect to the total number of variables in the model by considering the regular meshes $8 \times 12 \times 1$, $16 \times 24 \times 1$ and $24 \times 36 \times 1$. Furthermore, Fig. 13 plots the load-displacement curves of SFR8 and SFR8I obtained by the automatic load incrementation scheme and a 50 equal load increments scheme ($\text{NINC}^{\star} = 50$).

We remark that the non conforming element SFR8I presents approximately the same result as the quadratic

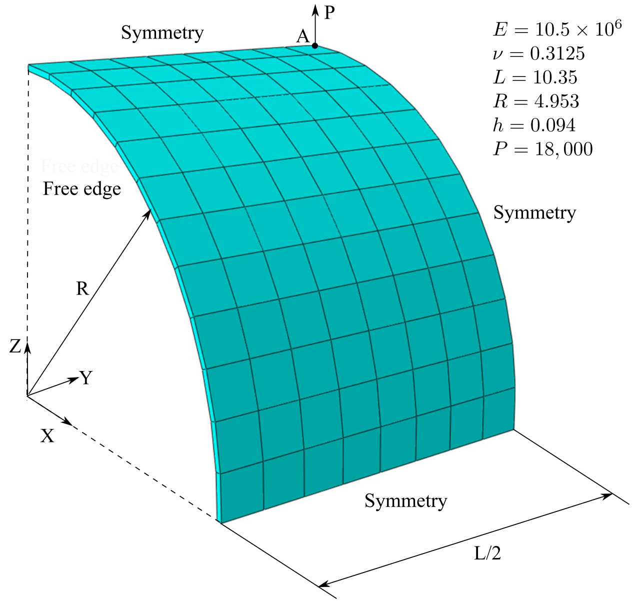

Fig. 10 One-eighth of the open-end cylindrical shell modeled with the regular mesh 8 × 12 × 1

Table 3 The open-end cylindrical shell

	C3D8	C3D20	SFR8	SFR8I
NINC	10	17	13	19
NITER	21	78	61	96

The total numbers of increments NINC and iterations NITER required to reach the ultimate solution with the automatic load incrementation scheme

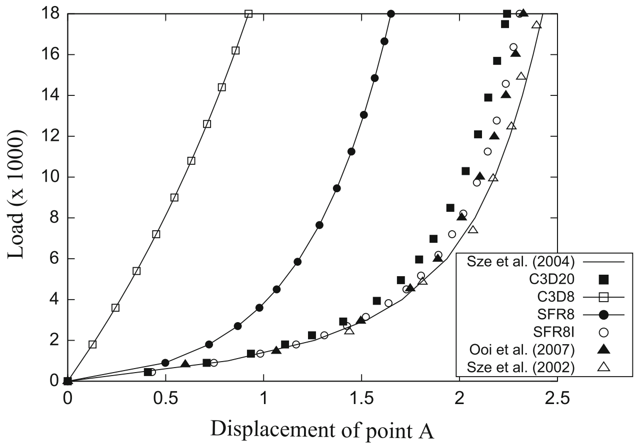

Fig. 11 Load-deflection curve of the open-end cylindrical shell

element US-HEXA20. SFR8I is more accurate than the quadratic element C3D20 and the solid-shell element HS is found to be the most accurate element in this example (with respect to the reference solution of Sze et al. [33]). In addition to that, we verify again in Fig. 13 that the SFR8 and SFR8I responses are practically not sensitive to load step size.

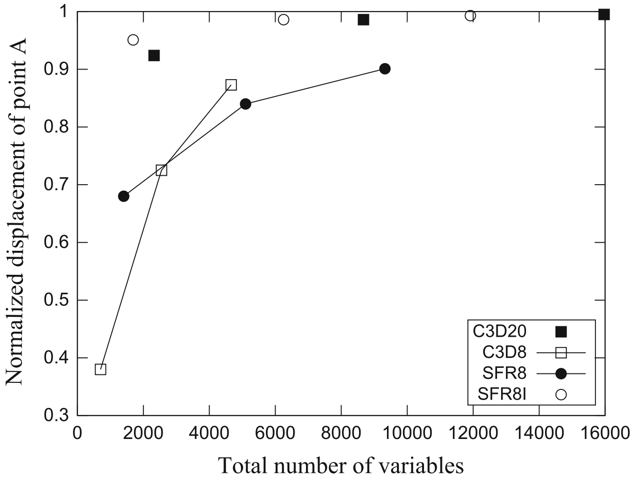

Fig. 12 The open-end cylindrical shell. Convergence of the normalized displacement of point A at $P = 18,000$ with respect to the total number of variables in the model ($w_A^{ref} = 2.425$ [33])

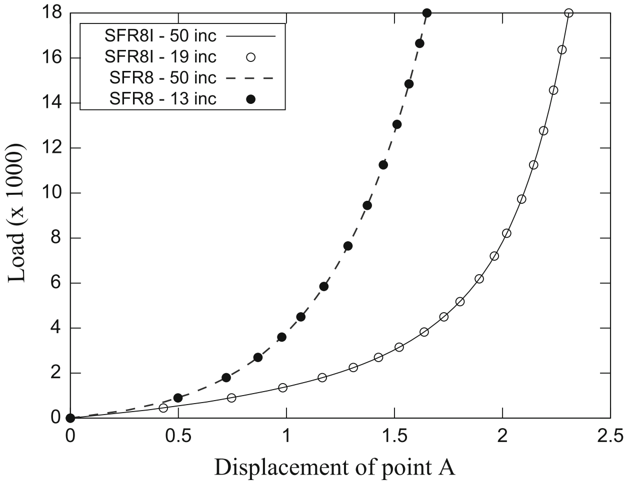

Fig. 13 The open-end cylindrical shell meshed with 8 × 12 × 1 elements. Impact of the load step size on the SFR8 and SFR8I load-displacement curves

4.4 Pinching of a clamped cylinder

We consider in this example a thin cylindrical shell fully clamped at one end and subjected to two opposite concentrated loads at the free end which are increased up to 1600. Owing to symmetry, only one-quarter of the cylinder is modeled with the regular mesh 16 × 16 × 1 as considered in the work of Fontes Valente et al. [16] (Fig. 14). We depict in Fig. 15 the load-displacement curves of the SFR concept hexahedral elements along with those of C3D8, C3D20 and the enhanced hexahedral element HCiS12 of Fontes Valente et al. [16]. All these results are compared with the reference curve of the four node shell element of Brank et al. [7] as taken in [16]. We summarize also in Table 4 the total numbers of increments NINC and iterations NITER required to

Fig. 14 One-fourth of the pinched clamped cylinder modeled with the regular mesh $16 \times 16 \times 1$

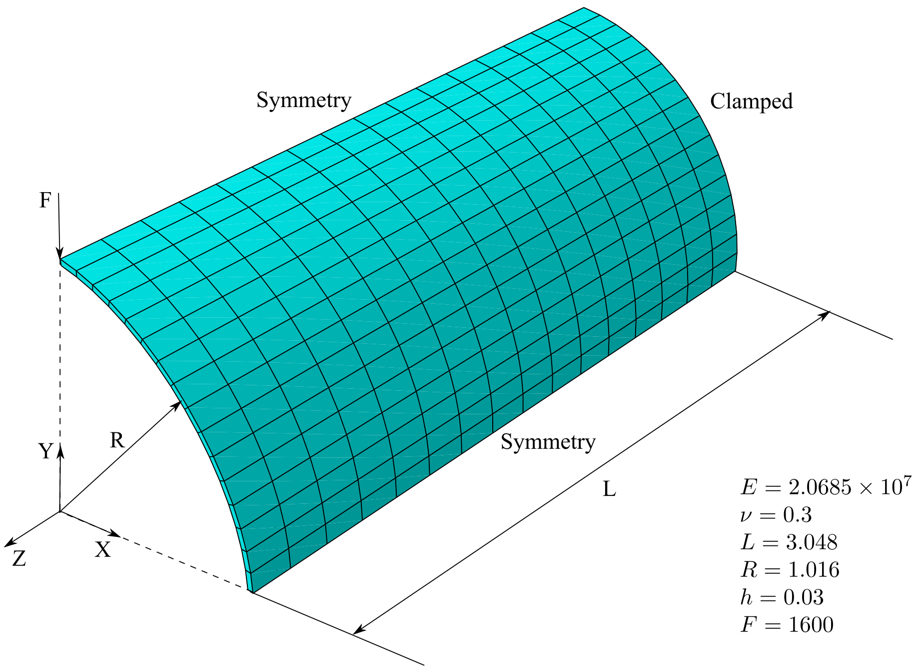

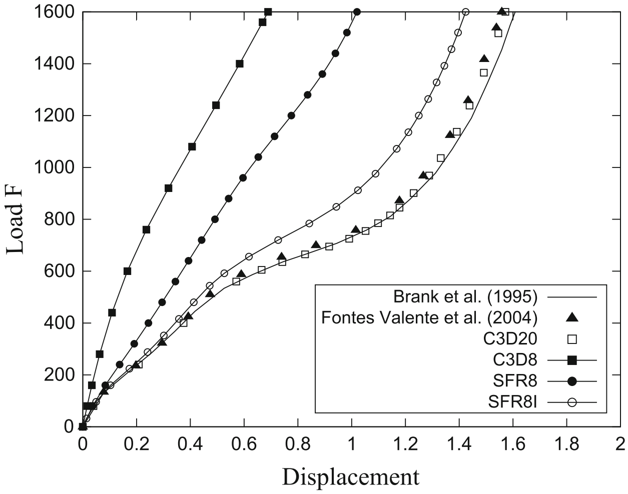

Fig. 15 Load-displacement curve of the pinched clamped cylindrical shell

Table 4 The pinched clamped cylinder

	C3D8	C3D20	SFR8	SFR8I
NINC	12	42	20	26
NITER	40	245	175	210

The total numbers of increments NINC and iterations NITER required to reach the ultimate solution with the automatic load incrementation scheme

obtain the ultimate solution with the automatic load incrementation scheme.

Contrary to the previous studied benchmarks, we remark in this example a notable difference between the results of SFR8I and C3D20 (this latter agrees well with the reference solution of Brank et al. [7]). This difference could be related to the adopted Total Lagrangian approach to describe the structure deformation (the Updated Lagrangian formulation is considered with C3D20 and HCiS12). A similar difference between the Updated and Total Lagrangian formulations has been already reported by Sze et al. [34] in some cases.

4.5 Slit annular plate under a line load

A slit annular plate with inner radius $R_1 = 6$, outer radius $R_2 = 10$ and thickness $h = 0.03$ is shown in Fig. 16. This plate is clamped at one end and subjected to a line force P at the other end that reaches 0.8 (force per unit length). The regular mesh $4 \times 40 \times 1$ is used to model the slit plate as depicted in Fig. 16. Reference solutions of the vertical deflections at points A and B (Fig. 16) are reported by Sze et al. [33] by using 10×80 S4R elements. The load-deflection curves of SFR8 and SFR8I are shown in Fig. 17 and compared to C3D8 and C3D20. Table 5 lists the total numbers of increments and iterations required to reach the ultimate solution when using the automatic load incrementation scheme.

As for the previous example, we remark that the result of SFR8I is different from C3D20 that better agrees with the reference curves.

4.6 A hinged cylindrical roof subjected to a central point load

A circular cylindrical roof subjected to a central point load is studied in this example. The longitudinal boundaries are

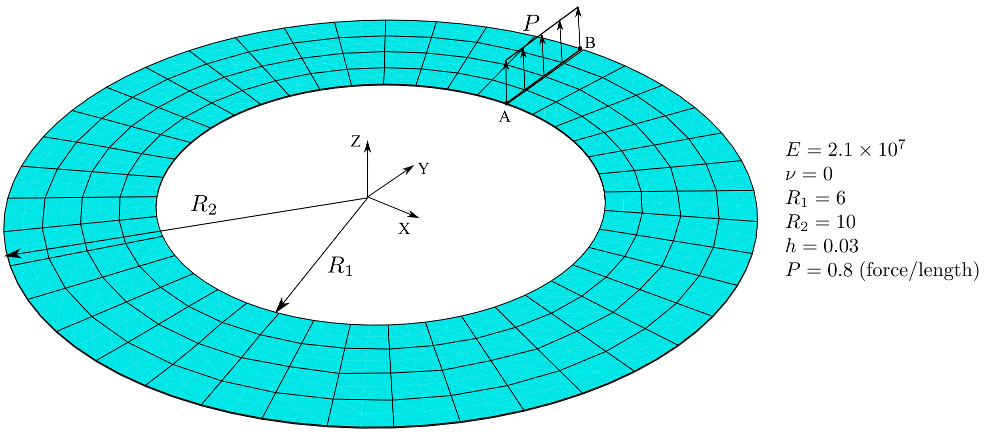

Fig. 16 The slit annular plate subjected to the line force P and modeled with the regular mesh $4 \times 40 \times 1$

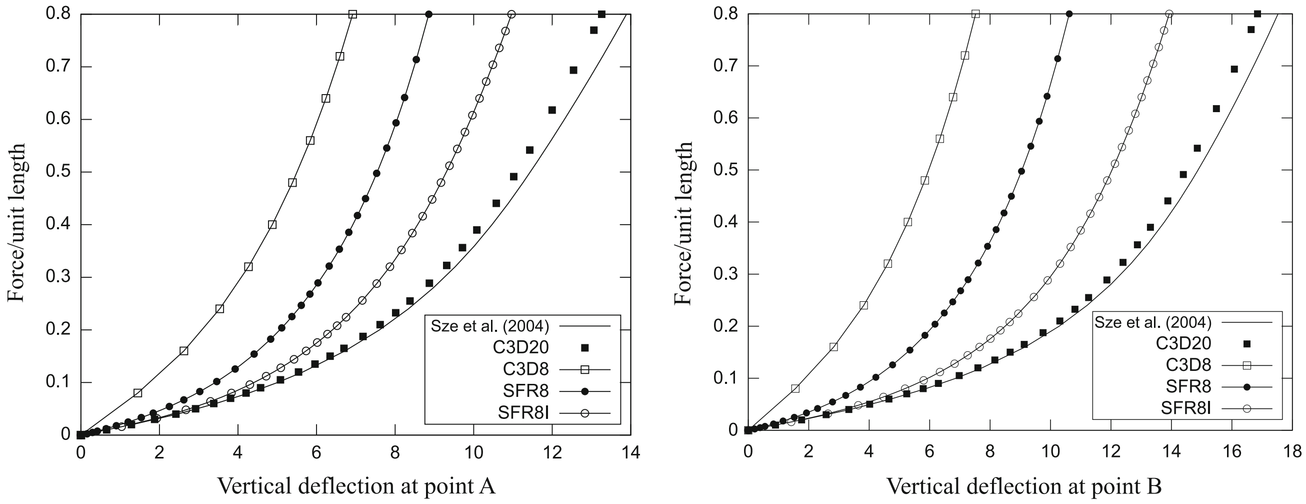

(a) **(b)**

Fig. 17 The slit annular plate. **a** Load-deflection at point A curve and **b** Load-deflection at point B curve

Table 5 The slit annular plate

	C3D8	C3D20	SFR8	SFR8I
NINC	10	29	31	32
NITER	34	161	170	185

The numbers of increments NINC and iterations NITER required to reach the ultimate solution with the automatic incrementation load scheme.

hinged and immovable while the curved edges are completely free. This benchmark constitutes a common assessment of the path following algorithm. Because of symmetry, only a quarter of the structure is modeled with the coarse regular mesh $4 \times 4 \times 2$ as used in the works of Schwarze and Reese [21] and Mostafa et al. [22] (Fig. 18). The use of two elements across the thickness permits to correctly represent hinged boundary conditions by fixing all translational DOFs of the mid-plane nodes as explained in [22]. The two thin and thick versions of this problem are considered ($h = 6.35$ and 12.7). These two cases were studied by Sze et al. in [33] by using converged regular meshes of S4R (8×8 and 16×16 for the thin shell and 16×16 and 24×24 for the thick roof). Due to the snapping behavior, this problem is solved by the arc-length method or the modified Riks method available in ABAQUS [32]. We show in Figs. 19 and 20 the load-displacement curves of SFR8 and SFR8I along with those of C3D20, the enhanced hexahedral element Q1STs of Schwarze and Reese [21] and the solid-shell element presented by Mostafa et al. in [22] (only for the thin shell). All these results are compared with those of S4R reported by Sze et al. in [33].

We remark that SFR8 and especially SFR8I predict correctly the unstable snap-back and snap-through behaviors of the thin and thick cylindrical roofs. It is worth noting that the C3D8 response was found to be divergent for the two cases and is not shown in Figs. 19 and 20 for clarity. In addition to

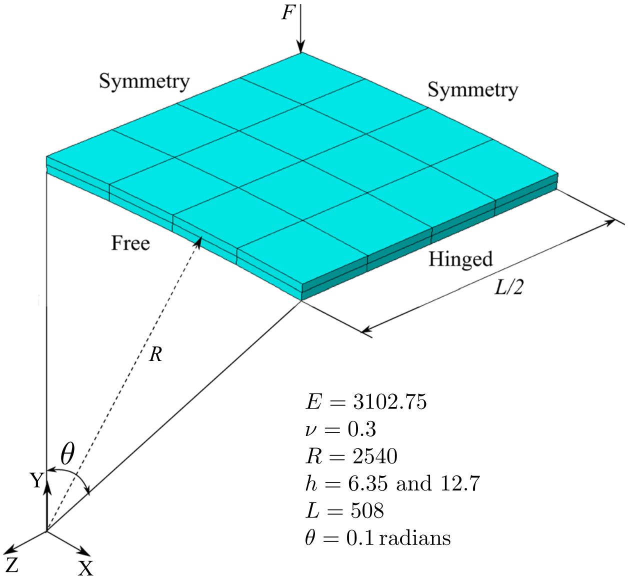

Fig. 18 One-fourth of the hinged cylindrical roof modeled with the regular mesh $4 \times 4 \times 2$

that, a good agreement between the SFR8I response, C3D20 and the other cited solutions is obtained.

5 Conclusion

In this paper, two recently published 3D solid elements presenting displacement and rotational DOFs were extended to account for geometric nonlinear problems. Their formulations are based on the so-called SFR concept that considers virtual rotations of a nodal fiber within the element enhancing the displacement vector approximation and the strain tensor expression. The geometric nonlinear formulation was developed within the framework of the Total Lagrangian approach that considers the Green–Lagrange strain tensor associated with the second Piola–Kirchoff stress tensor. These nonlinear hexahedral elements were implemented in the commercial code ABAQUS via the user element subroutine (UEL). To assess the performance of the proposed elements, several geometric nonlinear beam and shell benchmarks were analyzed and the obtained results were compared principally to the classical fully-integrated first-order and second-order hexahedral elements of ABAQUS (C3D8 and C3D20) as well as advanced solid finite elements from the literature.

The proposed SFR hexahedral elements were shown to clearly enhance the response of the classical first-order element C3D8 as in linear geometric problems. They were also found to predict correctly the studied beam and shell structures behaviors including snap-through and snap-back instabilities. The accuracy of the nonconforming element SFR8I was often close to that of the quadratic element C3D20 and the notable difference found in the pinched clamped cylinder and slit annular plate examples (Sects. 4.4 and 4.5) is likely to be related to the adopted Total Lagrangian approach that can lead, in some cases, to different results from the Updated Lagrangian formulation used in ABAQUS Standard.

For the future work, the Updated Lagrangian approach will be adopted in the SFR8 and SFR8I formulations and an evaluation of its impact on their accuracies will be addressed. Furthermore, the work presented in this paper deals exclusively with geometrically nonlinear problems with linear elastic behavior. Consequently, it would be interesting to extend the SFR8 and SFR8I formulations to account for material nonlinearity like elasto-plasticity. Besides, exten-

Fig. 19 Load-deflection curve of the thin hinged cylindrical roof

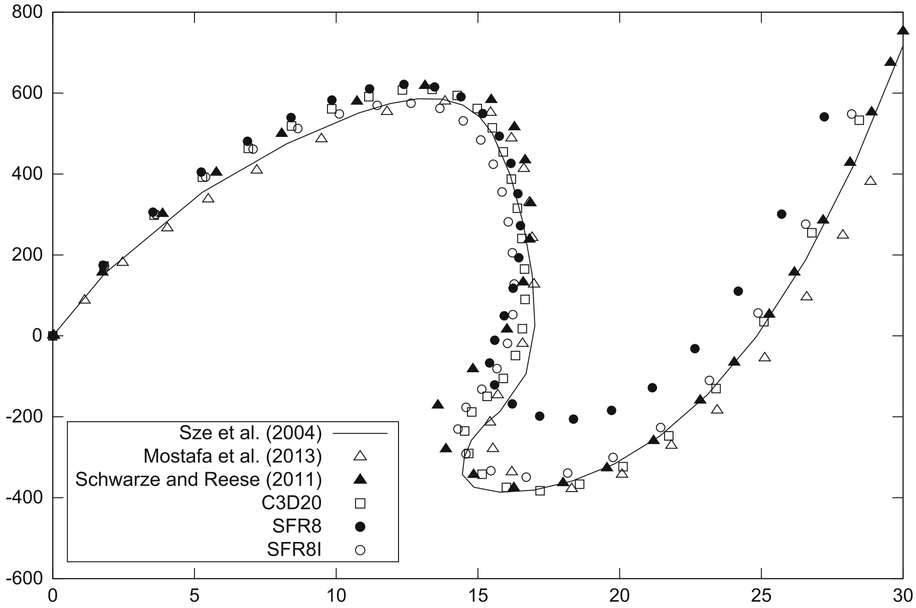

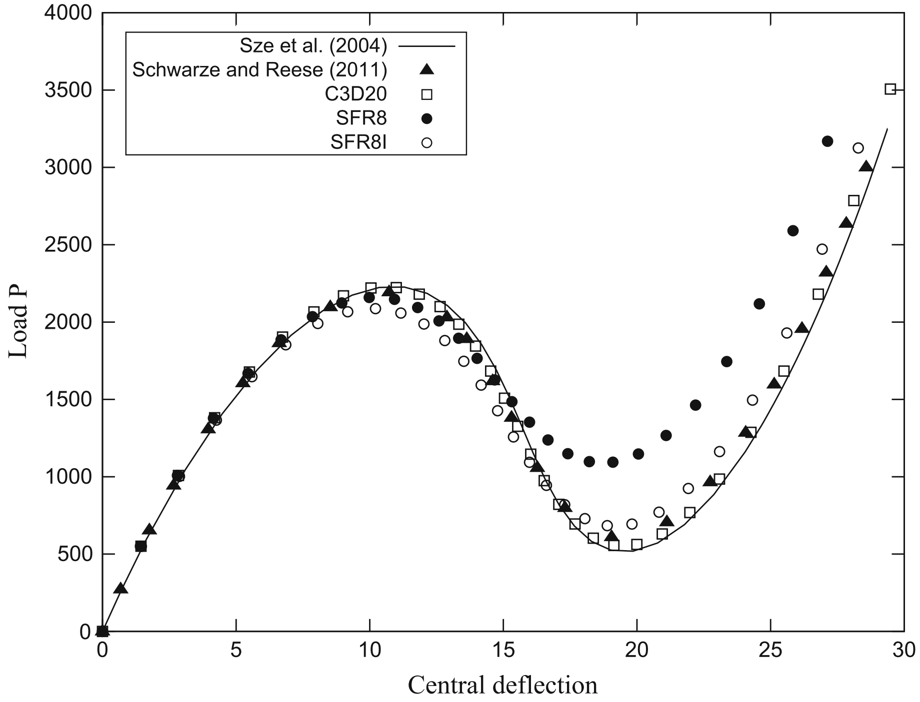

Fig. 20 Load-deflection curve of the thick hinged cylindrical roof

sion of the SFR concept elements is underway in order to analyze linear and nonlinear behaviors of composite laminate structures.

Appendix: Expressions of $[B_{L0}]$, $[B_{L1}]$ and $[B_{NL}]$

We use the following notation for partial derivatives:

$$\frac{\partial N_i}{\partial \alpha} = N_{i,\alpha}, \quad \alpha \equiv x, y, z$$

$$[B_{L0}] = \begin{bmatrix} & N_{i,x} & 0 & 0 & 0 & N_{i,x}(z-z_i) & -N_{i,x}(y-y_i) & \\ & 0 & N_{i,y} & 0 & -N_{i,y}(z-z_i) & 0 & N_{i,y}(x-x_i) & \\ & 0 & 0 & N_{i,z} & N_{i,z}(y-y_i) & -N_{i,z}(x-x_i) & 0 & \\ \cdots & N_{i,y} & N_{i,x} & 0 & -N_{i,x}(z-z_i) & N_{i,y}(z-z_i) & N_{i,x}(x-x_i)- & \cdots i=1,8 \\ & & & & & & N_{i,y}(y-y_i) & \\ & N_{i,z} & 0 & N_{i,x} & N_{i,x}(y-y_i) & N_{i,z}(z-z_i)- & -N_{i,z}(y-y_i) & \\ & & & & & N_{i,x}(x-x_i) & & \\ & 0 & N_{i,z} & N_{i,y} & N_{i,y}(y-y_i)- & -N_{i,y}(x-x_i) & N_{i,z}(x-x_i) & \\ & & & & N_{i,z}(z-z_i) & & & \end{bmatrix}$$

$$[B_{L1}] = \begin{bmatrix} & u_{,x}\cdot N_{i,x} & v_{,x}\cdot N_{i,x} & w_{,x}\cdot N_{i,x} & C_1 & C_2 & C_3 & \\ & u_{,y}\cdot N_{i,y} & v_{,y}\cdot N_{i,y} & w_{,y}\cdot N_{i,y} & C_4 & C_5 & C_6 & \\ & u_{,z}\cdot N_{i,z} & v_{,z}\cdot N_{i,z} & w_{,z}\cdot N_{i,z} & C_7 & C_8 & C_9 & \\ \cdots & u_{,x}\cdot N_{i,y}+u_{,y}\cdot N_{i,x} & v_{,x}\cdot N_{i,y}+v_{,y}\cdot N_{i,x} & w_{,x}\cdot N_{i,y}+w_{,y}\cdot N_{i,x} & C_{10} & C_{11} & C_{12} & \cdots i=1,8 \\ & u_{,z}\cdot N_{i,x}+u_{,x}\cdot N_{i,z} & v_{,z}\cdot N_{i,x}+v_{,x}\cdot N_{i,z} & w_{,z}\cdot N_{i,x}+w_{,x}\cdot N_{i,z} & C_{13} & C_{14} & C_{15} & \\ & u_{,y}\cdot N_{i,z}+u_{,z}\cdot N_{i,y} & v_{,y}\cdot N_{i,z}+v_{,z}\cdot N_{i,y} & w_{,y}\cdot N_{i,z}+w_{,z}\cdot N_{i,y} & C_{16} & C_{17} & C_{18} & \end{bmatrix}$$

with

$$C_1 = -v_{,x} \cdot N_{i,x}(z - z_i) + w_{,x} \cdot N_{i,x}(y - y_i);$$

$$C_2 = u_{,x} \cdot N_{i,x}(z - z_i) - w_{,x} \cdot \Big(N_{i,x}(x - x_i) + N_i\Big)$$

$$C_3 = -u_{,x} \cdot N_{i,x}(y - y_i) + v_{,x} \cdot \Big(N_{i,x}(x - x_i) + N_i\Big);$$

$$C_4 = -v_{,y} \cdot N_{i,y}(z - z_i) + w_{,y} \cdot \Big(N_{i,y}(y - y_i) + N_i\Big)$$

$$C_5 = u_{,y} \cdot N_{i,y}(z - z_i) - w_{,y} \cdot N_{i,y}(x - x_i) \quad ;$$

$$C_6 = -u_{,y} \cdot \Big(N_{i,y}(y - y_i) + N_i\Big) + v_{,y} \cdot N_{i,y}(x - x_i)$$

$$C_7 = -v_{,z} \cdot \Big(N_{i,z}(z - z_i) + N_i\Big) + w_{,z} \cdot N_{i,z}(y - y_i);$$

$$C_8 = u_{,z} \cdot \Big(N_{i,z}(z - z_i) + N_i\Big) - w_{,z} \cdot N_{i,z}(x - x_i)$$

$$C_9 = -u_{,z} \cdot N_{i,z}(y - y_i) + v_{,z} \cdot N_{i,z}(x - x_i)$$

$$\begin{aligned} C_{10} = {} & -v_{,x} \cdot N_{i,y}(z - z_i) - v_{,y} \cdot N_{i,x}(z - z_i) \\ & + w_{,x} \cdot \Big(N_{i,y}(y - y_i) + N_i\Big) + w_{,y} \cdot N_{i,x}(y - y_i) \end{aligned}$$

$$\begin{aligned} C_{11} = {} & u_{,x} \cdot N_{i,y}(z - z_i) + u_{,y} \cdot N_{i,x}(z - z_i) \\ & - w_{,x} \cdot N_{i,y}(x - x_i) - w_{,y} \cdot \Big(N_{i,x}(x - x_i) + N_i\Big) \end{aligned}$$

$$\begin{aligned} C_{12} = {} & -u_{,x} \cdot \Big(N_{i,y}(y - y_i) + N_i\Big) - u_{,y} \cdot N_{i,x}(y - y_i) \\ & + v_{,x} \cdot N_{i,y}(x - x_i) + v_{,y} \cdot \Big(N_{i,x}(x - x_i) + N_i\Big) \end{aligned}$$

$$\begin{aligned} C_{13} = {} & -v_{,x} \cdot \Big(N_{i,z}(z - z_i) + N_i\Big) - v_{,z} \cdot N_{i,x}(z - z_i) \\ & + w_{,x} \cdot N_{i,z}(y - y_i) + w_{,z} \cdot N_{i,x}(y - y_i) \end{aligned}$$

$$\begin{aligned} C_{14} = {} & u_{,x} \cdot \Big(N_{i,z}(z - z_i) + N_i\Big) + u_{,z} \cdot N_{i,x}(z - z_i) \\ & - w_{,x} \cdot N_{i,z}(x - x_i) - w_{,z} \cdot \Big(N_{i,x}(x - x_i) + N_i\Big) \end{aligned}$$

$$\begin{aligned} C_{15} = {} & -u_{,x} \cdot N_{i,z}(y - y_i) - u_{,z} \cdot N_{i,x}(y - y_i) \\ & + v_{,x} \cdot N_{i,z}(x - x_i) + v_{,z} \cdot \Big(N_{i,x}(x - x_i) + N_i\Big) \end{aligned}$$

$$\begin{aligned} C_{16} = {} & -v_{,y} \cdot \Big(N_{i,z}(z - z_i) + N_i\Big) - v_{,z} \cdot N_{i,y}(z - z_i) \\ & + w_{,y} \cdot N_{i,z}(y - y_i) + w_{,z} \cdot \Big(N_{i,y}(y - y_i) + N_i\Big) \end{aligned}$$

$$\begin{aligned} C_{17} = {} & u_{,y} \cdot \Big(N_{i,z}(z - z_i) + N_i\Big) + u_{,z} \cdot N_{i,y}(z - z_i) \\ & - w_{,y} \cdot N_{i,z}(x - x_i) - w_{,z} \cdot N_{i,y}(x - x_i) \end{aligned}$$

$$\begin{aligned} C_{18} = {} & -u_{,y} \cdot N_{i,z}(y - y_i) - u_{,z} \cdot \Big(N_{i,y}(y - y_i) + N_i\Big) \\ & + v_{,y} \cdot N_{i,z}(x - x_i) + v_{,z} \cdot N_{i,y}(x - x_i) \end{aligned}$$

$$[B_{NL}] = \begin{bmatrix} & N_{i,x} & 0 & 0 & 0 & N_{i,x}(z - z_i) & -N_{i,x}(y - y_i) & \\ & N_{i,y} & 0 & 0 & 0 & N_{i,y}(z - z_i) & -N_{i,y}(y - y_i) - N_i & \\ & N_{i,z} & 0 & 0 & 0 & N_{i,z}(z - z_i) + N_i & -N_{i,z}(y - y_i) & \\ & 0 & N_{i,x} & 0 & -N_{i,x}(z - z_i) & 0 & N_{i,x}(x - x_i) + N_i & \\ \cdots & 0 & N_{i,y} & 0 & -N_{i,y}(z - z_i) & 0 & N_{i,y}(x - x_i) & \cdots i = 1, 8 \\ & 0 & N_{i,z} & 0 & -N_{i,z}(z - z_i) - N_i & 0 & N_{i,z}(x - x_i) & \\ & 0 & 0 & N_{i,x} & N_{i,x}(y - y_i) & -N_{i,x}(x - x_i) - N_i & 0 & \\ & 0 & 0 & N_{i,y} & N_{i,y}(y - y_i) + N_i & -N_{i,y}(x - x_i) & 0 & \\ & 0 & 0 & N_{i,z} & N_{i,z}(y - y_i) & -N_{i,z}(x - x_i) & 0 & \end{bmatrix}$$

References

1. Ooi ET, Rajendran S, Yeo JH (2007) Extension of unsymmetric finite elements US-QUAD8 and US-HEXA20 for geometric nonlinear analyses. Eng Comput 24:407–431
2. Dvorkin EN, Bathe KJ (1984) A continuum mechanics based four-node shell element for general non-linear analysis. Eng Comput 1(1):77–88
3. Parisch H (1991) An investigation of a finite rotation four node assumed strain shell element. Int J Numer Methods Eng 31(1):127–150
4. Sansour C, Bufler H (1992) An exact finite rotation shell theory, its mixed variational formulation and its finite element implementation. Int J Numer Methods Eng 34(1):73–115
5. Wriggers P, Gruttmann F (1993) Thin shells with finite rotations formulated in biot stresses: Theory and finite element formulation. Int J Numer Methods Eng 36(12):2049–2071
6. Slavkovic R, Zivkovic M, Kojic M (1994) Enhanced 8-node three-dimensional solid and 4-node shell elements with incompatible generalized displacements. Commun Numer Methods Eng 10(9):699–709
7. Brank B, Damjanic F, Peric D (1995) On implementation of a nonlinear four node shell finite element for thin multilayered elastic shells. Comput Mech 16(5):341–359
8. Sansour C, Kollmann FG (2000) Families of 4-node and 9-node finite elements for a finite deformation shell theory. An assesment of hybrid stress, hybrid strain and enhanced strain elements. Comput Mech 24(6):435–447
9. Kuo-Mo H (1987) Nonlinear analysis of general shell structures by flat triangular shell element. Comput Struct 25(5):665–675
10. To CWS, Liu ML (1995) Hybrid strain based three node flat triangular shell elements-II. Numerical investigation of nonlinear problems. Comput Struct 54(6):1057–1076
11. Providas E, Kattis MA (1999) A simple finite element model for the geometrically nonlinear analysis of thin shells. Comput Mech 24(2):127–137
12. Kim JH, Kim YH (2002) A three-node C^0 ANS element for geometrically non-linear structural analysis. Comput Methods Appl Mech Eng 191:4035–4059
13. Andelfinger U, Ramm E (1993) EAS-elements for two-dimensional, three-dimensional, plate and shell structures and their equivalence to HR-elements. Int J Numer Methods Eng 36(8):1311–1337
14. Stander N, Matzenmiller A, Ramm E (1989) An assessment of assumed strain methods in finite rotation shell analysis. Eng Comput 6(1):58–66
15. Hauptmann R, Schweizerhof K (1998) A systematic development of solid-shell element formulations for linear and non-linear analyses employing only displacement degrees of freedom. Int J Numer Methods Eng 42(1):49–69
16. Fontes Valente RA, Alves de Sousa RJ, Natal Jorge RM (2004) An enhanced strain 3D element for large deformation elastoplastic thin-shell applications. Comput Mech 34:38–52
17. Vu-Quoc L, Tan XG (2003) Optimal solid shells for non-linear analyses of multilayer composites. I. Statics. Comput Methods Appl Mech Eng 192:975–1016
18. Alves de Sousa RJ, Cardoso RPR, Fontes Valente RA, Yoon JW, Gracio JJ, Natal Jorge RM (2006) A new one-point quadrature enhanced assumed strain (EAS) solid-shell element with multiple integration points along thickness-part II: nonlinear applications. Int J Numer Methods Eng 67(2):160–188
19. Klinkel S, Gruttmann F, Wagner W (2006) A robust non-linear solid shell element based on a mixed variational formulation. Comput Methods Appl Mech Eng 195:179–201
20. Abed-Meraim F, Combescure A (2009) An improved assumed strain solid-shell element formulation with physical stabilization for geometric non-linear applications and elastic-plastic stability analysis. Int J Numer Methods Eng 80(13):1640–1686
21. Schwarze M, Reese S (2011) A reduced integration solid-shell finite element based on the EAS and the ANS concept-Large deformation problems. Int J Numer Methods Eng 85(3):289–329
22. Mostafa M, Sivaselvan MV, Felippa CA (2013) A solid-shell corotational element based on ANDES, ANS and EAS for geometrically nonlinear structural analysis. Int J Numer Methods Eng 95(2):145–180
23. Klinkel S, Wagner W (1997) A geometrical non-linear brick element based on the EAS-method. Int J Numer Methods Eng 40(24):4529–4545
24. Simo JC, Armero F, Taylor RL (1993) Improved versions of assumed enhanced strain tri-linear elements for 3d finite deformation problems. Comput Methods Appl Mech Eng 110:359–386
25. Reese S (2005) On a physically stabilized one point finite element formulation for three-dimensional finite elasto-plasticity. Comput Methods Appl Mech Eng 194:4685–4715
26. Wang J, Wagoner RH (2005) A practical large-strain solid finite element for sheet forming. Int J Numer Methods Eng 63(4):473–501
27. Ayad R, Zouari W, Meftah K, Ben Zineb T, Benjeddou A (2013) Enrichment of linear hexahedral finite elements using rotations of a virtual space fiber. Int J Numer Methods Eng 95:46–70
28. Ayad R (2002) Contribution to the numerical modeling of solids and structures and the non-newtonian fluids forming process. Application to packaging materials (in French). Habilitation to conduct researches, University of Reims
29. Meftah K, Ayad R, Hecini M (2013) A new 3D 6-node solid finite element based upon the space fibre rotation concept. Eur J Comput Mech 22(1):1–29
30. Reddy JN (2004) An introduction to nonlinear finite element analysis. OUP, Oxford
31. Bischoff M, Ramm E (1997) Shear deformable shell elements for large strains and rotations. Int J Numer Methods Eng 40(23):4427–4449
32. ABAQUS (2014) Analysis user's manual. V. 6.14. ABAQUS Inc., Providence
33. Sze KY, Liu XH, Lo SH (2004) Popular benchmark problems for geometric nonlinear analysis of shells. Finite Elem Anal Des 40(11):1551–1569
34. Sze KY, Chan WK, Pian THH (2002) An eight-node hybrid-stress solid-shell element for geometric non-linear analysis of elastic shells. Int J Numer Methods Eng 55(7):853–878